Journal of
Materials Chemistry A

Li$_2$Ni$_{0.2}$Co$_{1.8}$O$_4$ having a Spinel Framework as Zero-Strain Positive Electrode Material for Lithium-Ion Batteries

Journal:	*Journal of Materials Chemistry A*
Manuscript ID	TA-ART-03-2019-003191.R1
Article Type:	Paper
Date Submitted by the Author:	26-Apr-2019
Complete List of Authors:	Ariyoshi , Kingo ; Osaka City University Graduate School of Engineering Faculty of Engineering Orikasa, Yuki; Ritsumeikan University, Department of Applied Chemistry kajikkawa, Kensuke; Osaka City University Yamada, Yusuke; Osaka City University, Applied Chemistry and Bioengineering

SCHOLARONE™
Manuscripts

ARTICLE

Li$_2$Ni$_{0.2}$Co$_{1.8}$O$_4$ having a Spinel Framework as Zero-Strain Positive Electrode Material for Lithium-Ion Batteries

Kingo Ariyoshi,[*a] Yuki Orikasa,[*b] Kensuke Kajikawa [a] and Yusuke Yamada [a]

Zero-strain insertion materials are ideal electrode materials for lithium-ion batteries because they do not undergo dimensional change during lithium insertion and extraction. Herein, a zero-strain insertion material, the Ni-substituted Li$_2$Co$_2$O$_4$ (Li$_2$Ni$_{0.2}$Co$_{1.8}$O$_4$) having a spinel framework, was synthesized and characterized to study the zero-strain mechanism. The change in the lattice dimension of Li$_2$Ni$_{0.2}$Co$_{1.8}$O$_4$ during lithium extraction was very small (only 0.1%), confirming that Li$_2$Ni$_{0.2}$Co$_{1.8}$O$_4$ is a zero-strain insertion material. It had a flat voltage profile at 3.5 V with a reversible capacity of 100 mAh g^{-1}, which was quite different from the voltage profile of LiCoO$_2$ having a layered structure. Detailed structural analysis by X-ray absorption spectroscopy revealed that there was no dimensional change because the changes in two crystallographic factors, contraction of the Co–O bond and distortion of the oxygen sublattice, cancelled out. The zero-strain lithium-ion battery combined with Li$_2$Ni$_{0.2}$Co$_{1.8}$O$_4$ and Li[Li$_{1/3}$Ti$_{5/3}$]O$_4$ showed good cycleability.

Introduction

In recent years, the use of lithium-ion batteries (LIBs) in electric vehicles and load-levelling power supplies, in addition to conventional applications, has been expected. Therefore, a fundamental life-extending technology for LIBs is important because these new applications require the battery life to be at least 10 years. An important factor in battery life is the structural stability of the electrode material. One such material used in LIBs, the lithium insertion material, undergoes a solid-state redox reaction involving the insertion or extraction of Li ions into or from the solid matrix without the destruction of the crystal structure framework. During these reactions, the transition metal ions constructing the crystal structure framework are oxidized and reduced, resulting in changes in their ionic radii. This induces the expansion or contraction of the crystal lattice, which is occasionally accompanied by lattice distortion.[1,2] Because lithium insertion materials made of transition metal oxides are typically brittle, the dimensional change causes particle fracture, leading to deterioration of the materials.[3-5]

Therefore, dimensional change in the crystal structure has to be avoided or minimized as much as possible to extend the cycle life of lithium insertion materials for long-life LIBs. Electrode materials exhibiting small dimensional change have superior cycleability because of their dimensional stability.[6-9] Hence, a zero-strain insertion material, which does not undergo dimensional change during lithium insertion/extraction, is an ideal electrode material. A representative example is lithium titanium oxide, Li[Li$_{1/3}$Ti$_{5/3}$]O$_4$ (LTO), which showed excellent cycleability.[10,11] Because its cycle life is unlimited, LTO has been used as a negative electrode in long-life LIBs[12-15] and a hybrid capacitor combined with a carbon-polarizable electrode.[16,17]

Thus far, only a few zero-strain materials have been reported.[18-26] These materials showed very small or no change in lattice dimension during lithium or sodium insertion/extraction. Their crystal structures have a large space that can accommodate Li ions, which effectively suppresses dimensional change during lithium insertion. However the volumetric energy density of these materials in terms of Wh dm^{-3} is relatively low owing to the large initial lattice volume. To apply a zero-strain material as a positive or negative electrode, one having closest-packed oxygen arrays is preferable because the low molar volume leads to a large volumetric capacity.[27]

In this study, we synthesized a novel zero-strain lithium insertion material, lithium cobalt oxide having a spinel framework with closest-packed oxygen array. The LiCoO$_2$ (LCO) having a spinel framework, a polymorph of lithium cobalt oxide, can be prepared at low temperature.[28-33] In this structure, Li ions are located at the octahedral sites. Among the transition-metal-substituted Li$_2$Co$_2$O$_4$ examined, a nickel-substituted material showed a reversible capacity of 100 mAh g^{-1} at 3.5 V with very small dimensional change. A zero-strain insertion mechanism was proposed on the basis of detailed structural analyses by powder X-ray diffraction (XRD) and X-ray absorption spectroscopy to determine factors responsible for the zero-strain phenomena, which are very useful information to design the zero-strain materials.

[a.] Department of Applied Chemistry and Bioengineering, Graduate School of Engineering, Osaka City University, Osaka, 558-8585, Japan
[b.] Department of Applied Chemistry, College of Life Sciences, Ritsumeikan University, 1-1-1 Noji-higashi, Kusatsu, Shiga 525-8577, Japan
*ariyoshi@a-chem.eng.osaka-cu.ac.jp; orikasa@fc.ritsumei.ac.jp

Results and discussion

Synthesis and electrochemical characterization of $Li_2M_{0.2}Co_{1.8}O_4$ (M = Ti–Zn).

Figure 1 shows the XRD patterns of $Li_2M_{0.2}Co_{1.8}O_4$ samples prepared via low-temperature synthesis. The Ti-, V-, Cu-, and Zn-substituted materials have impurity phases (marked by asterisks), i.e., TiO_2 (anatase), V_2O_5, CuO, and ZnO (wurtzite), the metal cations with di-, tera- or pentavalent were hardly substituted by trivalent Co ions. $Li_2Fe_{0.2}Co_{1.8}O_4$ was contaminated with $LiFe_5O_8$ and Li_2CO_3. This phase separation may result from difficulty for a formation of solid-solution between $LiCoO_2$ and $LiFeO_2$ due to instability of $LiFeO_2$ having a layered structure. No impurity phase can be seen for the Cr-, Mn-, and Ni-substituted samples because of the high stability of the trivalent state of their respective metal cations. The observed in the diffraction line located at $2\vartheta = 85°$, which provides a clear indication of the crystal symmetry (i.e., hexagonal or cubic lattice). This diffraction line is expected to separate into the 108 and 110 lines for the high-temperature phase (HT-phase) with a hexagonal lattice because of the anisotropy of the crystal lattice. On the other hand, the single diffraction line indexed by 440 is expected for the low-temperature phase (LT-phase) with a cubic lattice. The XRD pattern of $Li_2Mn_{0.2}Co_{1.8}O_4$ shows peak separation, suggesting that its crystal structure mainly contains a layered structure (HT-phase). The XRD patterns of the Fe-, Co-, and Zn-substituted samples show a shoulder peak at the low-angle region, indicating that a small amount of the layered phase is contaminated. Only the XRD patterns of the Cr- and Ni-substituted samples show a symmetric profile for the single 440 line, suggesting a predominantly spinel framework with a cubic lattice (LT-phase). The Cu-substituted sample also appears to have a cubic lattice despite the large amount of impurity phase. The lattice constants of the Cr- and Ni-substituted samples are

$8.00\underline{4}$ and $8.00\underline{8}$ Å, respectively. These values (ca. 8.00 Å) are the smallest lattice constants among those of lithium transition metal oxides having a spinel structure. This indicates that Co ions in the LT-phase are at the low-spin trivalent state, because the ionic radius of the trivalent Co ion at the low-spin state is the smallest among the 3d transition metal ions.

Quantitative analysis of the ratio between the spinel and layered phases is difficult owing to the broadening of the peak at 85°, which is caused by the low crystallinity obtained through low-temperature synthesis. The discharge profiles were thus utilized to estimate the amount of the LT-phase. Figure 2 shows the charge-discharge curves of the $Li/Li_2M_{0.2}Co_{1.8}O_4$ cells operated at a rate of 0.25 mA cm^{-2} in the voltage range of 2.5–4.2 V. In the discharge profile, the HT-phase has a sloping voltage profile at 3.9–4.2 V,[34] while the LT-phase has a flat one at 3.5 V.[29-31,35] In the charge profile, the voltage difference cannot be determined because of the larger polarization of the reaction for the LT-phase. The discharge profiles of all materials show a voltage plateau at 3.5 V, in addition to the reaction around 4 V, which differs in extent depending on the substituting cation. The reversible capacities of the Ti-, V-, and Zn-substituted samples smaller than those of the other samples suggest that the impurity phases are electrochemically inactive in the voltage range. The Fe-, Co-, and Zn-substituted samples, which have a shoulder peak corresponding to the 440 diffraction line in their XRD patterns, show a short voltage plateau at 3.5 V in addition to the large 4-V reaction. The Cr- and Ni-substituted samples, which have a dominant LT-phase, show a long voltage plateau at 3.5 V with large reversible capacity (>100 mAh g^{-1}) despite exhibiting a small discharge capacity between 3.9 and 4.2 V. The Cu-substituted sample also shows a long voltage plateau despite having an impurity phase. These results indicate that Cr and Ni-substituted $Li_2Co_2O_4$ ($Li_2Cr_{0.2}Co_{1.8}O_4$ and $Li_2Ni_{0.2}Co_{1.8}O_4$) have a dominant LT-phase and minor HT-phase without any impurity phase.
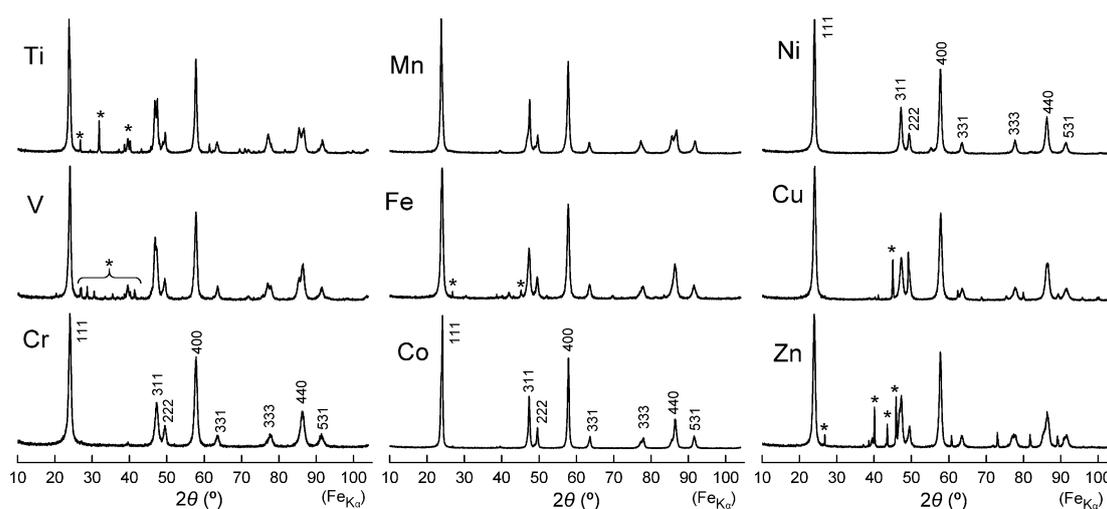

Fig. 1 XRD patterns of $Li_2M_{0.2}Co_{1.8}O_4$ (M = Ti–Zn) synthesized under air at 450°C for 16 h. Impurity phases are marked by asterisks.
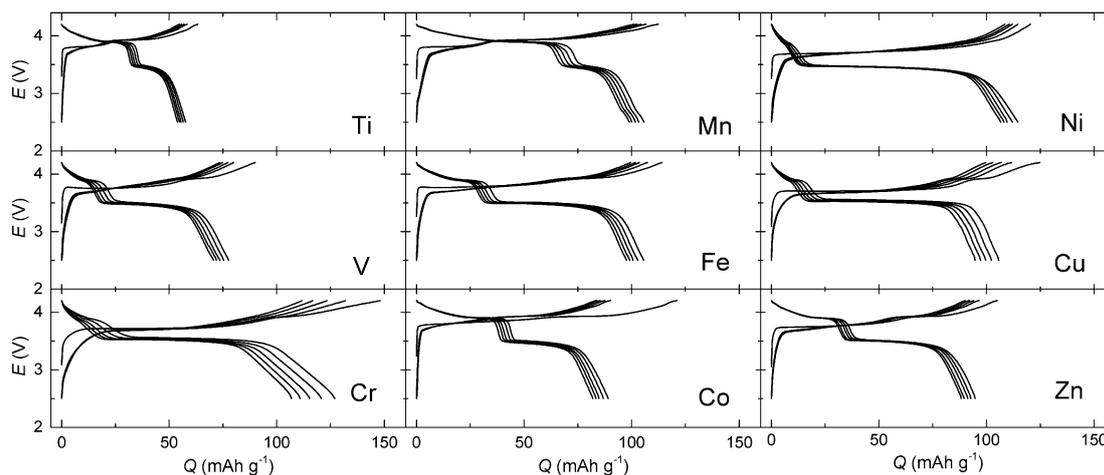
Fig. 2 Charge-discharge curves of Li/Li$_2$M$_{0.2}$Co$_{1.8}$O$_4$ (M = Ti–Zn) cells operated at a rate of 0.25 mA cm^{-2} in the voltage range of 2.5–4.2 V at 25°C for 5 cycles.
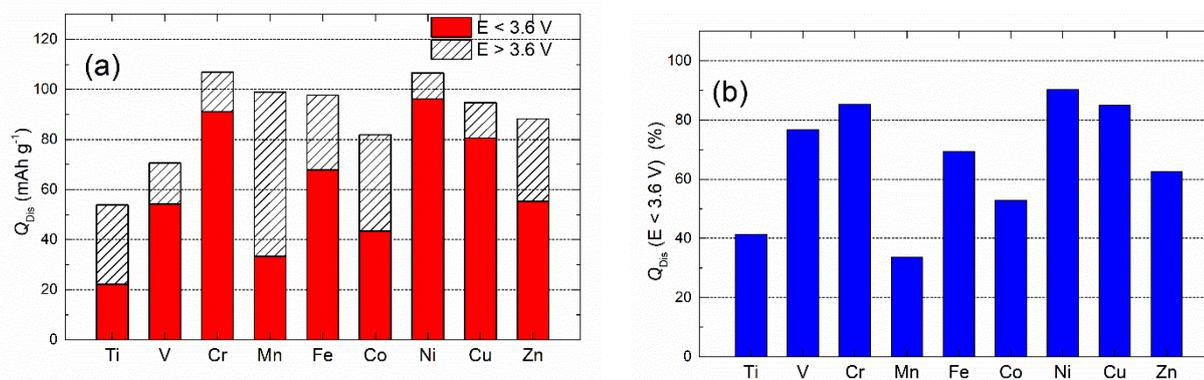

Fig. 3 (a) Discharge capacities (Q_{Dis}) of Li/Li$_2$M$_{0.2}$Co$_{1.8}$O$_4$ (M = Ti–Zn) cells at voltages (E) lower (red) and higher (shaded) than 3.6 V. (b) Ratio of the capacity (E < 3.6 V) to the total discharge capacity.

Figure 3a shows the summary of reversible capacities due to the reaction of the LT- and HT-phases, particularly the capacities at the 5th cycle. The amount of LT-phase in a material can be evaluated from the discharge capacity at voltages (E) below 3.6 V and that of the HT-phase from the discharge capacity at E > 3.6 V. The total capacity of a material, except for the Co- and Cu-substituted ones, roughly depends on the amount of impurity phase. Li$_2$Cu$_{0.2}$Co$_{1.8}$O$_4$, which has an impurity phase, delivers a larger capacity than that expected from the XRD pattern, while Li$_2$Co$_2$O$_4$ delivers a lower discharge capacity despite having no impurity phase, as shown in its XRD pattern. Among the materials, the Cr- and Ni-substituted ones show the highest discharge capacity at E < 3.6 V.

To compare the redox reaction potentials, the differential chronopotentiograms of Li$_2$Ni$_{0.2}$Co$_{1.8}$O$_4$ and HT-LCO were calculated from the charge-discharge curves (Figure 4). The oxidation and reduction peaks of Li$_2$Ni$_{0.2}$Co$_{1.8}$O$_4$ are located at 3.69 and 3.48 V, respectively. The peak separation of HT-LCO at 3.9 V is less than 0.05 V, while that of Li$_2$Ni$_{0.2}$Co$_{1.8}$O$_4$ is more than 0.2 V. From the open-circuit voltage measurements (Fig. S1), reversible potentials are almost constant at 3.6±0.03 V,

indicating that the reaction of Li$_2$Ni$_{0.2}$Co$_{1.8}$O$_4$ proceeds in a two-phase (heterogeneous) manner. The solid-state redox potential of Li$_2$Ni$_{0.2}$Co$_{1.8}$O$_4$ is 3.6 V lower than that of HT-LCO (3.9 V) by 0.3 V. The redox potentials of the two different phases (LT- and HT-phases) of Li$_2$Ni$_{0.2}$Co$_{1.8}$O$_4$ and HT-LCO are significantly different, indicating that solid-state redox potential of lithium insertion materials depends on the crystal structure in spite of the same redox couple of Co^{3+}/Co^{4+}.

The polarization observed in Fig. S1 increased significantly at both the end of charge and discharge. Thus it difficult to distinguish between the LT- and HT-phases in the charge profiles. A small voltage plateau due to the minor HT-phase was observed at ca. 4 V in the discharge profile. Therefore, the fraction of LT-phase can be estimated from the ratio of discharge capacity at E < 3.6 V to the total discharge capacity, $Q_{E<3.6V}$ / ($Q_{E<3.6V}$ + $Q_{E>3.6V}$), as shown in Figure 3b. Li$_2$Ni$_{0.2}$Co$_{1.8}$O$_4$ has the highest fraction of LT-phase among the samples. While its discharge profile show a longer voltage plateau, that of the Cr-substituted sample show a gradual decrease in operating voltage at the end of discharge. On the basis of these results, Li$_2$Ni$_{0.2}$Co$_{1.8}$O$_4$ was selected for the investigation of the reaction

mechanism of the LT-phase. The lithium insertion/extraction reactions of $Li_2Ni_{0.2}Co_{1.8}O_4$ proceed according to the equation,

$Li_2Ni_{0.2}Co_{1.8}O_4 \rightleftharpoons Li_{2-x}Ni_{0.2}Co_{1.8}O_4 + xLi^+ + xe^-$.

Theoretical capacity of $Li_2Ni_{0.2}Co_{1.8}O_4$ based on the above equation is 274 mAh g^{-1}. Because the fraction of LT-phase in $Li_2Ni_{0.2}Co_{1.8}O_4$ (%LT) is 90.2% as calculated from the discharge capacity below 3.6 V. Thus, actual theoretical capacity of the $Li_2Ni_{0.2}Co_{1.8}O_4$ containing HT- and impurity phases is lower than the Q_{calc}, i.e., $Q_{calc} \times$ %LT. Therefore, the amount of the Li extracted from $Li_2Ni_{0.2}Co_{1.8}O_4$ (x in $Li_{2-x}Ni_{0.2}Co_{1.8}O_4$) can be calculated using the equation,

$x = 2 \times Q_{E<3.6V}/(Q_{calc} \times$ %LT),

where $Q_{E<3.6V}$ is the observed capacity at $E < 3.6$ V (96.2 mAh g^{-1} from Figure 3a), Q_{calc} is the theoretical capacity (274 mAh g^{-1}), and %LT is the fraction of LT-phase in $Li_2Ni_{0.2}Co_{1.8}O_4$ (90.2%). Using this equation, $x = 0.78$, that is, almost half of the Li ions is extracted from Ni-substituted $Li_2Co_2O_4$ in the LT-phase.
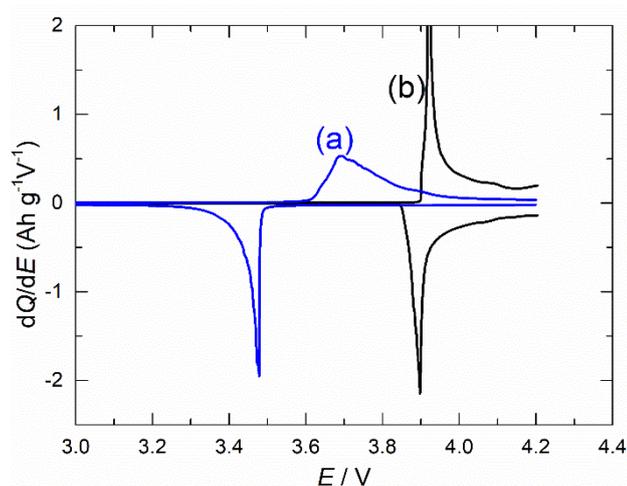

Fig. 4 Differential chronopotentiograms (dQ/dE) calculated from the charge-discharge curves of (a) $Li/Li_2Ni_{0.2}Co_{1.8}O_4$ and (b) Li/HT-$LiCoO_2$ cells at the 2nd cycle.

Structural change in $Li_2Ni_{0.2}Co_{1.8}O_4$ during lithium extraction.

The change in the $Li_2Ni_{0.2}Co_{1.8}O_4$ crystal structure after charging was examined by ex-situ XRD (Figure 5). There is no peak shift in the XRD pattern, suggesting that the lattice dimension does not change significantly. The spinel framework, consisting of the CoO_6 octahedra connected by edge sharing, is maintained (i.e., a topotactic reaction). The cubic lattice constant changes from 8.00$\underline{5}$ Å to 7.99$\underline{6}$ Å. The changes in the lattice constant and volume are only 0.1% and 0.4%, respectively, which are much smaller than those for other materials having a spinel structure.[36,37,44,45] The intensities of the 400 and 440 lines decrease, while those of the other diffraction lines are almost the same, because of the rearrangement of Li ions in the crystal structure during lithium extraction.

To investigate the change in the $Li_2Ni_{0.2}Co_{1.8}O_4$ crystal structure during lithium extraction, structural analysis was carried out using three structural models: one at the initial state and the other two at the charged state (Figure 6). Because the spinel framework constructed by the transition metal (mainly

Co^{3+}) and oxygen ions is maintained during the reaction, the difference is the location of the Li ions. The structural model at the initial state has a spinel framework wherein Li ions are located at the octahedral 16c sites in space group Fd-3m. All octahedral 16c and 16d sites are occupied by Li and transition metal ions, respectively, implying an ordered rock-salt structure with an ordering different from that of a layered structure. The crystal structure is similar to that of other lithium insertion materials having a spinel structure after lithium insertion reaction. Thus, this model is called the "reduced-spinel" model.[28-30] The two structural models at the charged state can be constructed using different locations for the Li ions: one with Li ions randomly distributed at half of the octahedral 16c sites (i.e., site occupancy of 0.5) after lithium extraction, and the other is a spinel structure wherein Li ions fully occupy the tetrahedral 8a sites.
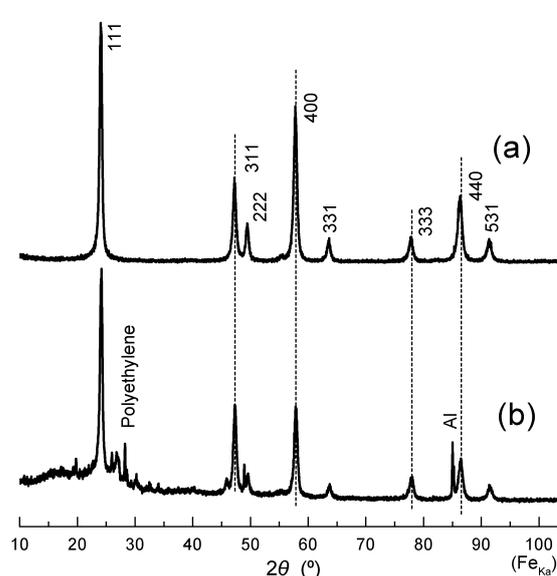

Fig. 5 XRD patterns of (a) pristine $Li_2Ni_{0.2}Co_{1.8}O_4$ synthesized under air at 400°C for 6 days and (b) $Li_{1.22}Ni_{0.2}Co_{1.8}O_4$ electrode obtained by charging to 4.2 V (114 mAh g^{-1} of charge capacity). The cubic lattice parameters are 8.00$\underline{5}$ and 7.99$\underline{6}$ Å for (a) $Li_2Ni_{0.2}Co_{1.8}O_4$ and (b) $Li_{1.22}Ni_{0.2}Co_{1.8}O_4$, respectively.

Remarkably, the locations of the Li ions at the tetrahedral 8a or octahedral 16c sites affect the integrated intensities of the 311 and 400 diffraction lines (I_{311} and I_{400}, respectively). With increasing occupancy of the 8a sites, I_{311} increases; similarly, I_{400} increases with increasing occupancy of the 16c sites. Hence, the locations of the Li ions in the spinel framework can be identified by comparing the calculated and observed integrated intensity ratio, I_{311}/I_{400}. Figure 7 shows the I_{311}/I_{400} calculated using the structural models shown in Figure 6, as well as the observed values obtained from XRD analysis (Figure 5). The observed I_{311}/I_{400} at the initial state (0.54) is very close to that calculated using the model based on the reduced-spinel model (Figure 6a). This structural identification conforms well with previously reported structural refinement.[28-30] For the charged state of $Li_2Ni_{0.2}Co_{1.8}O_4$, the observed I_{311}/I_{400} from different independent observations is 0.94. This is similar to the I_{311}/I_{400} calculated
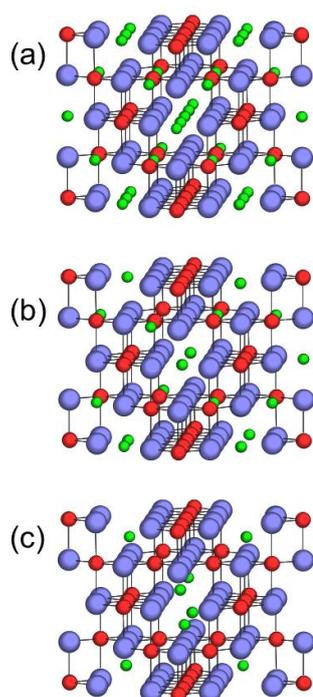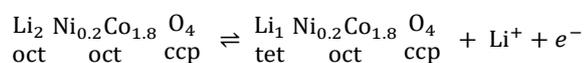
Fig. 6 Schematic illustrations of the $Li_2Ni_{0.2}Co_{1.8}O_4$ crystal structure at the (a) initial and (b, c) charged states. Blue, red and green spheres indicate O, Co, and Li ions, respectively. Li ions occupy either (a) all octahedral 16c sites, (b) half of the 16c sites, or (c) all tetrahedral 8a sites.

Fig. 7 Ratio of the integrated intensities of the 311 and 400 diffraction lines (I_{311}/I_{400}) of $Li_2Ni_{0.2}Co_{1.8}O_4$ as a function of oxygen positional parameter u for three structural models having a spinel framework. Closed circles indicate the calculated intensity ratios for the three models shown in Figure 6 [Li ions occupying all octahedral 16c sites (blue), half of the 16c sites (black), or all tetrahedral 8a sites (red)]. Dashed lines represent the observed intensity ratio of $Li_2Ni_{0.2}Co_{1.8}O_4$ before (blue) and after (red) charging.

using the spinel model (Figure 6c) and significantly different from that calculated using the random distribution model (Figure 6b). Based on these results, lithium insertion/extraction of $Li_2Ni_{0.2}Co_{1.8}O_4$ can be expressed as

$$\underset{oct}{Li_2}\ \underset{oct}{Ni_{0.2}Co_{1.8}}\ \underset{ccp}{O_4} \rightleftharpoons \underset{tet}{Li_1}\ \underset{oct}{Ni_{0.2}Co_{1.8}}\ \underset{ccp}{O_4} + Li^+ + e^-$$

The crystal structure of $Li_2Ni_{0.2}Co_{1.8}O_4$ is similar to that of $Li_2Mn_2O_4$ formed by lithium insertion of $LiMn_2O_4$,[37] except for the crystal symmetry, which is cubic for the LT-phase and tetragonal for $Li_2Mn_2O_4$. During lithium extraction, Li ions occupying the octahedral sites in $Li_2Ni_{0.2}Co_{1.8}O_4$ are extracted, while the remaining ones migrate to the tetrahedral sites. After lithium extraction, all Li ions are located at the tetrahedral sites. $Li_2Ni_{0.2}Co_{1.8}O_4$ is reversibly transformed from the reduced-spinel to the spinel structure during the reaction.

The charge compensation mechanism of $Li_2Ni_{0.2}Co_{1.8}O_4$ was analysed by X-ray absorption near edge structure. Figure 8 shows the Co and Ni K-edge spectra of pristine and charged $Li_2Ni_{0.2}Co_{1.8}O_4$ with that of HT-LCO as reference. The Co K-edge spectrum is shifted toward higher energy after charging $Li_2Ni_{0.2}Co_{1.8}O_4$, indicating that cobalt is oxidized by the charging reaction. Comparison with $Li_{1-x}CoO_2$ reference samples[38] shows that the valence state of cobalt is approximately 3.5. In addition, the white line in the Ni K-edge spectrum is shifted to higher energy, indicating the oxidation of the Ni ion. Although the Co and Ni 3d orbitals are hybridized, the contribution of charge compensation between Co and Ni cannot be accurately determined.
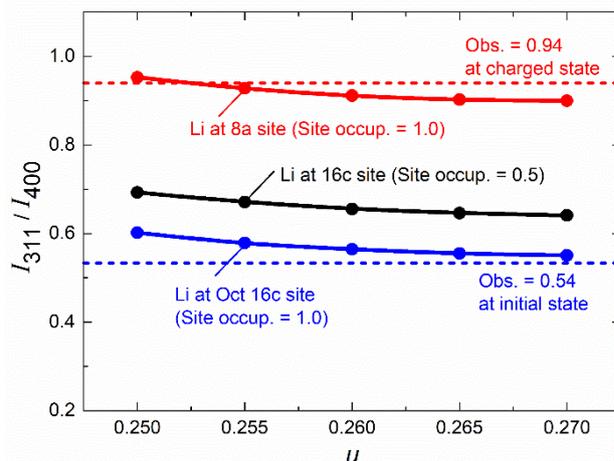
The local structure was analysed by EXAFS. Co K-edge EXAFS was used because the Co atomic ratio is relatively high and thus reflects the average changes in $Li_2Ni_{0.2}Co_{1.8}O_4$. Figure 9 shows the Fourier transforms of the Co K-edge EXAFS oscillations of pristine and charged $Li_2Ni_{0.2}Co_{1.8}O_4$ and HT-LCO. The EXAFS oscillations of these samples are provided in Figure S2. The first main peak at ~1.8 Å correlates to the hexacoordinated Co–O shell, while the second one (~2.5 Å) corresponds to the contribution of the Co–Co shell. Refined parameters obtained from curve fittings of the Co K-edge EXAFS oscillations are summarized in Table S1. The inverse Fourier transform spectra of the simulated curves are identical to experimental data, indicating that the fitting is performed correctly (Figure S3). Multiplying the Co‑Co distance (second coordination) by $2\sqrt{2}$ yields a value that agrees well with the lattice constant. For the charging reaction, the Co–O bond is shortened, indicating the decrease in the Co ionic radius upon oxidation, in which valence increases from 3 to 3.5. This trend is the same as in the case of HT-LCO.[38] On the other hand, the Co–Co distance remains constant which is a characteristic of the zero-strain phenomena in $Li_2Ni_{0.2}Co_{1.8}O_4$. The Co–Co distance in HT-LCO was reported to decrease as the interlayer distance decreased upon lithium extraction.[39] In contrast, no change in the Co–Co distance is observed in $Li_2Ni_{0.2}Co_{1.8}O_4$. This agrees well with XRD data showing that the lattice constant upon Li extraction does not changed. Although the Co ionic radius and Co–O bond length decrease, the Co–Co distance does not significantly change; thus, the lattice constant also does not change.
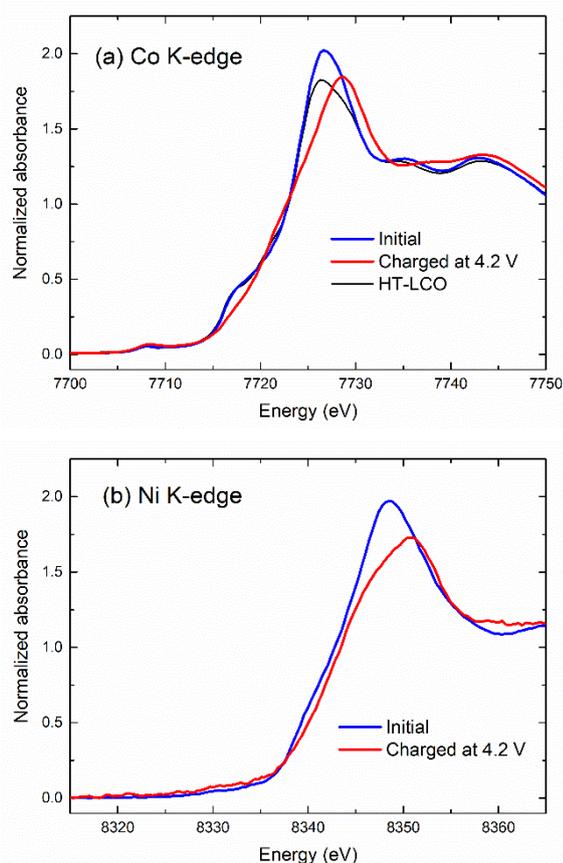
Fig. 8 (a) Co and (b) Ni *K*-edge XANES spectra of Li$_2$Ni$_{0.2}$Co$_{1.8}$O$_4$ at the initial and charged states. The Co *K*-edge XANES spectrum of LiCoO$_2$ (LCO) having a layered structure is also shown for comparison.
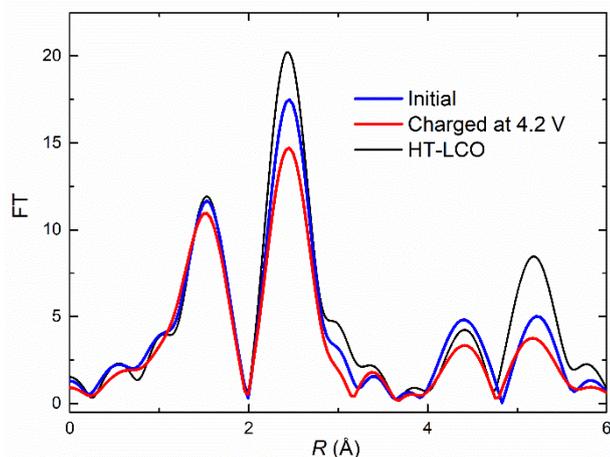

Fig. 9 Fourier transforms of the Co *K*-edge EXAFS spectra of Li$_2$Ni$_{0.2}$Co$_{1.8}$O$_4$ at the initial and charged states. The Co *K*-edge EXAFS spectrum of LiCoO$_2$ (LCO) having a layered structure is also shown for comparison.

Zero-strain insertion mechanism of Li$_2$Ni$_{0.2}$Co$_{1.8}$O$_4$.

The oxygen sublattice in the spinel framework has a cubic close-packed arrangement. Oxygen anions in the spinel framework usually deviate from their ideal positions. This deviation is expressed as a single parameter *u*, the so-called oxygen positional parameter. It implies changes in the bond lengths, bond angles, and symmetries of the CoO$_6$ octahedra.[40]

Figure 10 shows the relationship between *u*, ranging from 0.25 (the ideal position) to 0.27, and the Co–O bond length at a specific cubic lattice parameter *a*, which is 8.00 Å. The Co–O bond length varies with *u* even though a remains constant. This means that *u* increases when the Co–O bond length changes to keep a constant, which explains the zero-strain insertion phenomenon in Li$_2$Ni$_{0.2}$Co$_{1.8}$O$_4$. During lithium extraction, the Co–O bond length decreases owing to the contraction of the Co ionic radius from 0.545 Å at the trivalent state to 0.53 Å at the octahedral tetravalent state. Oxygen anions leave the vacant octahedral sites (16c sites in space group Fd-3m) along the <111> direction simultaneously because the Co–O attraction strengthens with the increased positive charge of Co ions during lithium extraction.

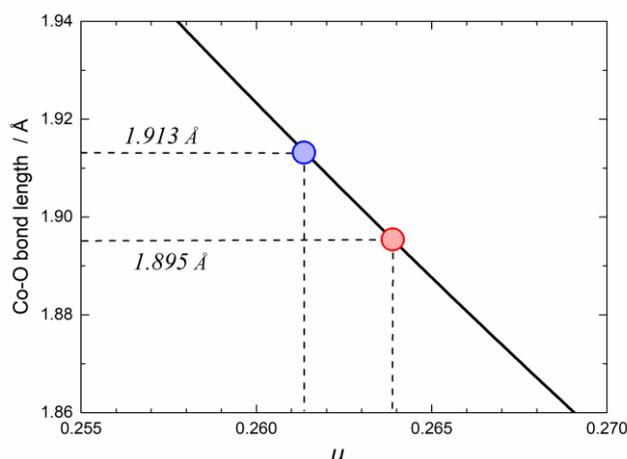**Fig. 10** Relationship between oxygen positional parameter *u* and Co–O bond length *l* given by $l = a \sqrt{\left(\frac{1}{2} - u\right)^2 + 2\left(u - \frac{1}{4}\right)^2}$, where *a* is the lattice parameter. The black line shows the relationship for *a* = 8.00 Å. The blue and red circles denote the values for Li$_2$Co$_{1.8}$Ni$_{0.2}$O$_4$ before and after lithium extraction, respectively, determined from EXAFS analysis.

A crystallographic illustration of the zero-strain insertion mechanism of Li$_2$Ni$_{0.2}$Co$_{1.8}$O$_4$ is depicted in Figure 11. The crystal plane of the spinel framework along the [100] axis is shown with greater emphasis on oxygen sublattice distortion. The yellow square indicates the unit cell of each structure. Distortion of the oxygen sublattice induces the reduction of the site symmetry of the CoO$_6$ octahedra from O_h to D_{3d} in the spinel framework with space group Fd-3m. The distortion of the CoO$_6$ octahedra becomes larger with increasing *u*, leading to a decrease in the O–Co–O bond angle from 84.3° at the initial state to 83.1° after charging. Consequently, the unit cell dimension does not change despite the contraction of the Co–O bond during lithium extraction in Li$_2$Ni$_{0.2}$Co$_{1.8}$O$_4$. The zero-strain insertion mechanism of Li$_2$Ni$_{0.2}$Co$_{1.8}$O$_4$ can be explained by accounting for a reversible change in *u* during the reaction, the so-called an oxygen-swing model observed in LTO.[11]
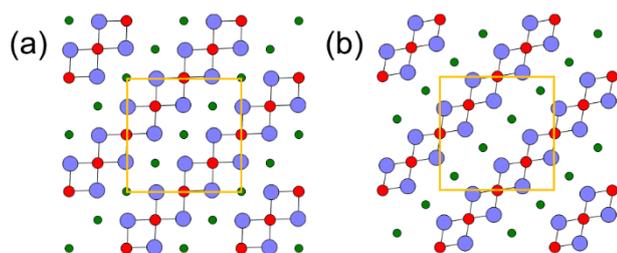
Fig. 11 Schematic illustrations of the $Li_2Ni_{0.2}Co_{1.8}O_4$ crystal structure viewed along [100] direction (a) before and (b) after charging. Blue, red, and green spheres indicate O, Co, and Li ions, respectively. A yellow square indicates the cubic unit cell, which does not change in size owing to the zero-strain mechanism.

Finally, a cycleability test was carried out for the zero-strain lithium-ion battery of $LTO/Li_2Ni_{0.2}Co_{1.8}O_4$ in which both electrode materials are zero-strain to assess its structural stability. Figure 12 shows the charge-discharge curves of the $LTO/Li_2Ni_{0.2}Co_{1.8}O_4$ cell. The cell was charged to constant capacity (80 mAh g^{-1}) to avoid the reaction of the small amount of HT-phase at the 4-V region and discharged to 1.0 V at a rate of 0.77 mA cm^{-2} (1 C-rate). The polarization on charge was slightly increased during 30 cycles. The increase in polarization on charge is more apparent at higher current density (Fig. S4). On the contrary, polarization on discharge was almost constant and the charge capacity at each cycle was fully delivered even at high rate (1 C-rate). X-ray fluorescence analysis indicated that phosphorus compounds derived from PF_6^- ions deposited on the separator of the cell after the cycle tests. Thus, the polarization increase on charge was explained by the clogging of the separator with the phosphorous compounds, not by deterioration of $Li_2Ni_{0.2}Co_{1.8}O_4$. XRD examination was performed for the $Li_2Ni_{0.2}Co_{1.8}O_4$ electrode after 50 cycles to confirm structural stability (Figure S5). The obtained XRD pattern was virtually identical to that before cycling in terms of life positions and intensity ratios. In addition, full width at half maximum (FWHM) of diffraction lines before and after cycling were the same (0.62° for the 400 line), indicating that no change in grain size during cycling. This result is inevitable for the zero-strain $Li_2Ni_{0.2}Co_{1.8}O_4$ because of very low internal stress produced by the minimal dimensional change of the crystal structure. These results indicate that the cycleability and rate capability of $Li_2Ni_{0.2}Co_{1.8}O_4$ can be expected to be as excellent as that of zero-strain LTO.

The volumetric capacity and dimensional change of zero-strain $Li_2Ni_{0.2}Co_{1.8}O_4$ was compared with those of other lithium insertion materials (Figure 13).[10,18-20,24,36,40-44] All zero-strain materials except LTO has a crystal structure with a large space that can accommodate Li ions. Such a large space is expected to reduce lattice distortion during lithium insertion/extraction, leading to a small dimensional change. However, the volumetric capacities of the materials are relatively low owing to their large lattice volumes. On the contrary, $Li_2Ni_{0.2}Co_{1.8}O_4$ has a dense crystal lattice because of the cubic closed-packed oxygen array, which allows compatibility between large volumetric capacity and small dimensional change.
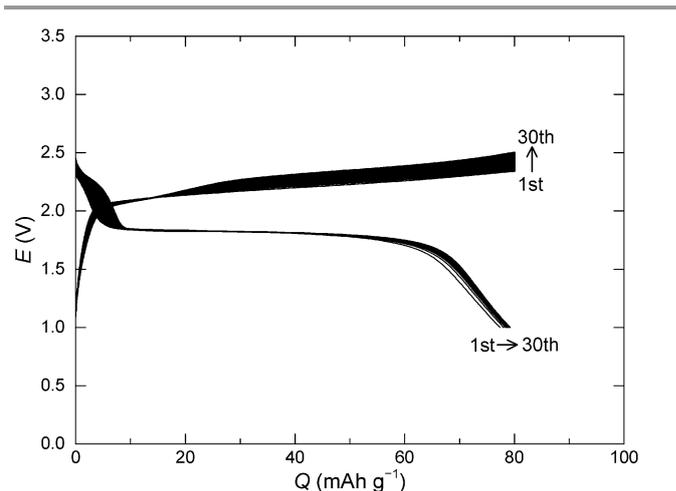

Fig. 12 Charge-discharge curves of a zero-strain lithium-ion battery of $LTO/Li_2Co_{1.8}Ni_{0.2}O_4$ operated at a rate of 0.77 mA cm^{-2} at 25°C for 30 cycles. The charge capacity was set to a constant capacity of 80 mAh g^{-1}.
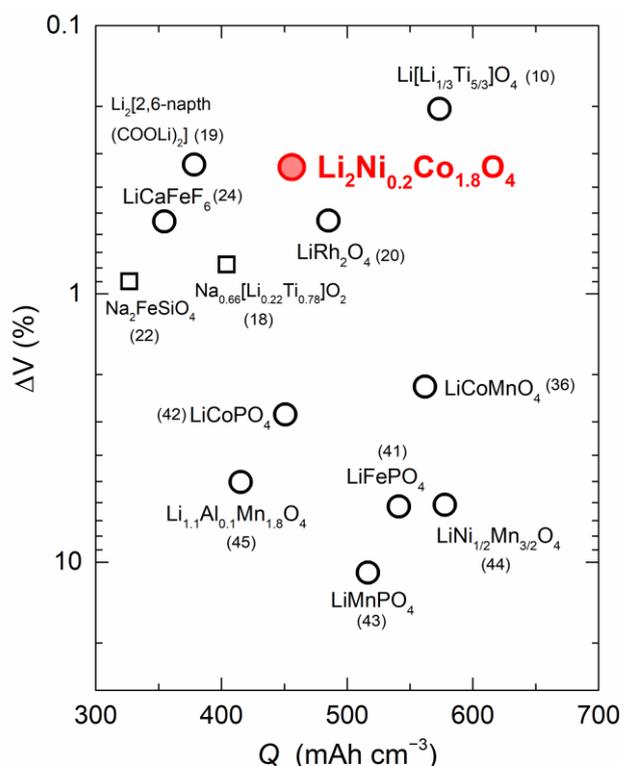

Fig. 13 Change in volume and volumetric capacity of $Li_2Co_{1.8}Ni_{0.2}O_4$ and other lithium insertion materials. The numbers in parentheses indicate the references for these data.

Experimental

Material synthesis and characterization.

$Li_2M_{0.2}Co_{1.8}O_4$ (M = Ti–Zn) was prepared by a solid-state synthetic method. A reaction mixture of Li_2CO_3, $Co(OH)_2$ and another 3d transition metal source [i.e., TiO_2, V_2O_5, Cr_2O_3, MnOOH (manganite), FeOOH (goethite), $Ni(NO_3)_2$, CuO or ZnO] was heated at 450°C for 16 h under air in a tubular electric furnace. The synthesized materials were characterized by powder XRD using an X-ray diffractometer (LabX XRD-6100,

Shimadzu Corp., Japan) equipped with a graphite monochromator using Fe Kα radiation operated at 40 kV and 15 mA. Data were collected from $2\vartheta = 9°$ to $2\vartheta = 104°$ at a scan rate of 0.5° min^{-1}. The change in the $Li_2Ni_{0.2}Co_{1.8}O_4$ crystal structure after charging up to 4.2 V was also characterized by ex-situ XRD.

Electrochemical measurements.

The structure of the electrochemical cell used for material testing was previously reported.[36] To prepare the positive electrode, a black viscous slurry consisting of 88 wt% of $Li_2M_{0.2}Co_{1.8}O_4$ (M = Ti–Zn), 6 wt% of acetylene black, and 6 wt% of polyvinylidene fluoride dispersed in N-methyl-2-pyrrolidone was cast onto an aluminium foil. N-methyl-2-pyrrolidone was evaporated at 80°C for 1 h under vacuum, and the electrode was dried under vacuum at 150°C overnight. Finally, the electrode was punched out to form a disk (16.0 mm diameter). The loading weight of the electrode mix was ca. 15 mg cm^{-2}. The Li metal electrode was used as the negative electrode. The electrolyte used was 1 M $LiPF_6$ dissolved in a 3:7 (v/v) ethylene carbonate/dimethyl carbonate solution (Kishida Chemical Co., Ltd., Japan). Electrochemical tests for the cells were carried out using a battery cycler (Battery Laboratory System, Keisokuki Center Co., Ltd., Japan).

X-ray absorption measurements by synchrotron radiation.

Charged/discharged electrodes of $Li_2M_{0.2}Co_{1.8}O_4$ (M = Ti–Zn) were removed from the cell in a glove box. The dried electrodes were sealed in laminated packets in an argon-filled glove box. The Co and Ni *K*-edge spectra were recorded at beam line BL01B1 of the SPring-8 synchrotron radiation facility of the Japanese Synchrotron Radiation Research Institute (Harima, Japan). Measurements were performed in transmission mode using a Si(111) monochromator. The energy scale was calibrated using Cu and Co foils. All data were collected at room temperature. Extended X-ray absorption fine structure (EXAFS) structural analysis was performed using the REX2000 (ver. 2.6) data analysis software, and theoretical backscattering phases and amplitudes were calculated with code FEFF8.

Conclusions

Among the transition-metal-substituted $Li_2Co_2O_4$ ($Li_2M_{0.2}Co_{1.8}O_4$, M = 3d transition metals) prepared by low-temperature synthesis at 450°C, the Cr- and Ni-substituted ones had a reduced-spinel structure wherein the lithium and transition metal ions were ordered at the octahedral sites. The materials showed a flat voltage profile at 3.5 V with a reversible capacity of 100 mAh g^{-1}, which is different from that of HT-LCO having a layered structure. Based on ex-situ XRD experiments, $Li_2Ni_{0.2}Co_{1.8}O_4$ was converted to $LiNi_{0.2}Co_{1.8}O_4$ having a spinel structure during lithium extraction with negligibly small dimensional change (~0.1 %), indicating that it is a zero-strain insertion material. Detailed structural analysis by X-ray absorption spectroscopy showed that during lithium extraction, the Co–Co bond length remains constant, while the Co–O bond length decreases owing to the change in the Co ionic radius. The zero-strain phenomenon can be explained by the oxygen-swing model, in which the displacement of oxygen anions plays an important role as a buffer against the contraction of the Co–O bond during lithium extraction. Zero-strain $Li_2Ni_{0.2}Co_{1.8}O_4$ has a reduced-spinel structure with a closest-packed oxygen array, which is denser than the structures of other zero-strain positive electrode materials reported thus far. Therefore, in $Li_2Ni_{0.2}Co_{1.8}O_4$, a large volumetric capacity and small dimensional change can be compatible, leading to long cycle life. Zero-strain lithium-ion battery of LTO/$Li_2Ni_{0.2}Co_{1.8}O_4$ was firstly demonstrated which has potentially excellent cycleability, because both electrodes are zero-strain materials.

Conflicts of interest

There are no conflicts to declare.

Acknowledgements

References

1   M. S. Whittingham, *Chem. Rev.*, 2004, **104**, 4271.
2   B. L. Ellis, K. T. Lee and L. F. Nazar, *Chem. Mater.*, 2010, **22**, 691.
3   D. Wang, X. Wu, Z. Wang and L. Chen, *J. Power Sources*, 2005, **140**, 125.
4   P. Yan, J. Zheng, M. Gu, J. Xiao, J. G. Zhang and C. M. Wang, *Nat. Commun.*, 2017, **8**, 14101.
5   J. Christensen and J. Newman, *J. Solid State Electrochem.*, 2006, **10**, 293.
6   T. A. Arunkumar and A. Manthiram, *Electrochem. Solid-State Lett.*, 2005, **8**, A403.
7   A. Manthiram, J. Choi and W. Choi, *Solid State Ionics*, 2006, **177**, 2629.
8   W. H. Woodford, W. C. Carter and Y.-M. Chiang, *J. Electrochem. Soc.*, 2014, **161**, F3005.
9   D. Chen, D. Kramer and R. Monig, *Electrochim. Acta*, 2018, **259**, 939.
10 T. Ohuku, A. Ueda and N. Yamamoto, *J. Electrochem. Soc.*, 1995, **142**, 1431.
11 K. Ariyoshi, R. Yamato and T. Ohzuku, *Electrochim. Acta*, 2005, **51**, 1125.
12 N. Takami, K. Yoshida and Y. Harada, *J. Electrochem. Soc.*, 2017, **164**, A6254.
13 N. Takami, H. Inagaki, Y. Tatebayashi, H. Saruwatari, K.; Honda and S. Egusa, *J. Power Sources*, 2013, **244**, 469.
14 I. Belharouak, Y.-K. Sun, W. Lu and K. Amine, *J. Electrochem. Soc.*, 2007, **154**, A1083.
15 K. Ariyoshi, S. Yamamoto and T. Ohzuku, *J. Power Sources*, 2003, **119–121**, 959.
16 G. G. Amatucci, F. Badway, A. D. Pasquier and T. Zheng, *J. Electrochem. Soc.*, 2001, **148**, A930.
17 A. D. Pasquier, I. Plitz, S. Menocal and G. Amatucci, *J. Power Sources*, 2003, **115**, 171.
18 Y. Wang, X. Yu, S. Xu, J. Bai, R. Xiao, Y.-S. Hu, H. Li, X.-Q. Yang, L. Chen and X. Huang, *Nat. Commun.*, 2013, **4**, 2365.

19 N. Ogihara, T. Yasuda, Y. Kishida, T. Ohsuna, K. Miyamoto and N. Ohba, *Angew. Chem., Int. Ed.*, 2014, **53**, 11467.

20 A. Nakamura, Y. Gu, K. Taniguchi, N. Shibata, H. Takagi and Y. Ikuhara, *Chem. Mater.*, 2015, **27**, 938.

21 J. A. Hill, A. B. Cairns, J. J. K. Lim, S. J. Cassidy, S. J. Clarke and A. L. Goodwin, *Cryst. Eng. Comm.*, 2015, **17**, 2925.

22 S. Li, J. Guo, Z. Ye, X. Zhao, S. Wu, J.-X. Mi, C.-Z. Wang, Z. Gong, M. J. McDonald, Z. Zhu, K.-M. Ho and Y. Yang, *ACS Appl. Mater. Interfaces*, 2016, **8**, 17233.

23 Z. Ye, X. Zhao, S. Li, S. Wu, P. Wu, M. C. Nguyen, J. Guo, J. Mi, Z. Gong, Z.-Z. Zhu, Y. Yang, C.-Z. Wang and K.-M. Ho, *Electrochim. Acta*, 2016, **212**, 934.

24 L. Biasi, G. Lieser, C. Drager, S. Indris, J. Rana, G. Schumacher, R. Monig, H. Ehrenberg, J. R. Binder and H. Gesswein, *J. Power Sources*, 2017, **362**, 192.

25 J. Kim, G. Yoon, M. H. Lee, H. Kim, S. Lee and K. Kang, *Chem. Mater.*, 2017, **29**, 7826.

26 H. Zhang, D. Buchholz and S. Passerini, *Energies*, 2017, **10**, 889.

27 T. Ohzuku and A. Ueda, *Solid State Ionics*, 1994, **69**, 201.

28 R. J. Gummow, D. C. Liles and M. M. Thackeray, *Mater. Res. Bull.*, 1993, **28**, 235.

29 R. J. Gummow and M. M. Thackeray, *J. Electrochem. Soc.*, 1993, **140**, 3365.

30 E. Rossen, J. N. Reimers and J. R. Dahn, *Solid State Ionics*, 1993, **62**, 53.

31 R. Yazami, N. Lebrun, M. Bonneau and M. Molteni, *J. Power Sources*, 1995, **54**, 389.

32 B. Garcia, J. Farcy and J. P. Pereira-Ramos, *J. Electrochem. Soc.*, 1997, **144**, 1179.

33 Y. Shao-Horn, S. A. Hackney, A. J. Kahaian and M. M. Thackeray, *J. Solid State Chem.*, 2002, **168**, 60.

34 T. Ohzuku and A. Ueda, *J. Electrochem. Soc.*, 1994, **141**, 2972.

35 E. Lee, J. Blauwkamp, F. C. Castro, J. Wu, V. P. Dravid,; P. Yan; C. Wang; S. Kim; C. Wolverton, R. Benedek, F. Dogan, J. S. Park, J. R. Croy and M. M. Thackeray, *ACS Appl. Mater. Interfaces*, 2016, **8**, 27720.

36 K. Ariyoshi, H. Yamamoto and Y. Yamada, *Electrochim. Acta*, 2018, **260**, 498.

37 T. Ohzuku, M. Kitagawa and T. Hirai, *J. Electrochem. Soc.*, 1990, **137**, 769.

38 Y. Orikasa, D. Takamatsu, K. Yamamoto, Y. Koyama, S. Mori, T. Masese, T. Mori, T. Minato, H. Tanida, T.; Uruga, Z. Ogumi and Y. Uchimoto, *Adv. Mater. Interfaces*, 2014, **1**, 1400195.

39 J. T. Hertz, Q. Huang, T. McQueen, T. Klimczuk, J. W. G. Bos, L. Viciu and R. J.Cava, *Phys. Rev. B*, 2008, **77**, 075119.

40 K. E. Sickafus and J. M. Wills, *J. Am. Ceram. Soc.*, 1999, **82**, 3279.

41 A. K. Padhi, K. S. Nanjundaswamy and J. B. Goodenough, *J. Electrochem. Soc.,* 1997, **144**, 1188.

42 K. Amine, H. Yasuda and M. Yamachi, *Electrochem. Solid-State Lett.,* 2000, **3**, 178.

43 G. Li, H. Azuma and M. Tohda, *Electrochem. Solid-State Lett.,* 2002, **5**, A135.

44 K. Ariyoshi, Y. Iwakoshi, N. Nakayama and T. Ohzuku, *J. Electrochem. Soc.*, 2004, **151**, A296.

45 K. Ariyoshi, E. Iwata, M. Kuniyoshi, H. Wakabayashi and T. Ohzuku, *Electrochem. Solid-State Lett.*, 2006, **9**, A557.